Spatial and Temporal Distribution of Solar Green-Line Corona for Solar Cycles 18 – 24

Jouni Takalo[1] (ID)

Abstract

The homogeneous coronal data set (HCDS) of the green corona (Fe XIV) and the coronal index of solar activity (CI) have been used to study the time–latitudinal distribution in Solar Cycles 18 – 24 and compared with similar distribution of sunspots, the magnetic fields, and the solar 10.7 cm radio flux. The most important results are: i) the distribution of coronal intensities related to the cycle maximum are different for individual cycles, ii) the poleward migration of the HCDS from mid-latitudes in each cycle exists, even in the extremely weak Cycle 24, and the same is valid for the equatorward migration, iii) the overall values of HCDS are slightly stronger for the northern hemisphere than for the southern one, iv) the distribution of the HDCS is in coincidence with the strongest photospheric magnetic fields ($B > 50$ Gauss) and histograms of the sunspot groups, v) the Gnevyshev gap was confirmed with at least 95% confidence in the CI, however with different behavior for odd and even cycles. Principal component analysis (PCA) showed that the first and second components account for 87.7% and 7.3% of the total variation of the CI. Furthermore, the second PCA component of the green corona was quite different for Cycle 21, compared with other cycles.

Keywords Sun: Solar corona · Sun: Sunspot groups · Methods: Distribution analysis · Statistical analysis

1. Introduction

Th green 530.3 nm (Fe XIV) line is the most prominent coronal irradiance indicator. Its importance is due to its existence all over the solar limb and the interconnection to the local strength of the magnetic fields of the Sun (Rušin and Rybanský, 2002). This line originates at a temperature of about 2 million K. Its first casual observations were made soon after the invention of a coronagraph in 1939 at the Arosa observatory by Waldmeier (1957); more systematic observations started in 1946 at several coronal stations worldwide (Minarovjech, Rušin, and Saniga, 2011b). Quite continuous measurements of green corona thus exist for Solar Cycles 18 – 23. In addition, there now exist data for Solar Cycle 24 (Lukáč and Rybanský, 2010).

✉ J. Takalo
jojuta@gmail.com

1   Space Physics and Astronomy Research Unit, University of Oulu, POB 3000, FIN-90014, Oulu, Finland

Kane (2015) dealt with the similarities and differences of the coronal index of solar activity (CI) and sunspot numbers (SSN) using normalized indices. He states that both have very similar shape in the ascending and maximum phases of the solar cycle, but differ in the descending phase of the cycle. This is due to the varying abundance of coronal holes in the descending phase of the cycles. Cycles 19 and 22 are most identical in the shape of their CI and SSN parameters. Cycles 18 and 23 have excess CI compared to SSN, and Cycles 20 and 21 have excess CI but located at the end of the descending phase. This shows that the shape of the CI is not related to the 22-year Hale cycle.

Another question arises: does the corona exhibit the so-called Gnevyshev gap (GG), which has been reported in many solar phenomena (Gnevyshev, 1977; Feminella and Storini, 1997; Ahluwalia and Kamide, 2004; Bazilevskaya, Makhmutov, and Sladkova, 2006; Kane, 2008; Norton and Gallagher, 2010; Du, 2015; Takalo and Mursula, 2018, 2020) and even in the geomagnetic indices (Takalo, 2021b). This has not been reported previously. Rybanský, Rušin, and Minarovjech (2001), however, stated that the existence of double maxima, as found by Gnevyshev (1967) was not confirmed in the corona index (CI). Single peaks of the CI were observed mostly in coincidence with sunspot numbers, even though some time shift could occur with a comparison with sunspot number, e.g. of two years in Cycle 21.

This article is organized as follows: Section 2 presents the data and methods used in this article. In Section 3 we study spatial and temporal statistics using the homogeneous coronal data set (HCDS), i.e. 72 values with five-degree resolution around the solar limb starting from the North Pole and circulating counterclockwise (see more in Section 2). In Section 4 we explore the coronal index of solar activity (CI) in order to find clues about GG in the corona, and we compare sunspot numbers and solar radio flux to CI using principal component analysis (PCA). We discuss the results and give our conclusions in Section 5.

2. Data and Methods

2.1. Corona Indices

The homogeneous coronal data set (HCDS) is the irradiance of the Sun as a star in the coronal green line (Fe XIV, 530.3 nm). It is derived from ground-based observations of the green corona made by the network of coronal stations (Kislovodsk, Lomnický Štít, Norikura, and Sacramento Peak). These indices are, however, no longer measured in the traditional way as was done earlier at Lomnický Štít Observatory (formerly Lomnický Štít coronal station). The coronal intensities have been measured at 72 points at five-degree separation starting from the North Pole counterclockwise around the Sun at a height of around 50 arcsec. The values are calibrated to the center of the solar disk to obtain absolute values of intensity, i.e. absolute coronal units (ACU). One ACU represents the intensity of the continuous spectrum of the center of the solar disk in a passband of one Ångström at the same wavelength as the observed coronal spectral line (1 ACU $= 3.89$ W m^{-2} sr^{-1} at 530.3 nm). We refer to these data later sometimes as "the latitudinal corona index".

Rybanský (1975) introduced the coronal index of solar activity (CI) as a general index of solar activity. CI, a full-disk index, represents the averaged daily irradiance emitted through the green coronal line into one steradian towards the Earth. It is expressed in power units [W sr^{-1}] as measured from a ground-based observatory. The idea is that these values can be transferred to other units in order to compare them to spacecraft measurements. The monthly values of CI are between $2-20 \times 10^{16}$ W sr^{-1}, and daily values have, thus far, always been

Table 1 Sunspot-cycle lengths and dates [fractional years, and year and month] of (starting) sunspot minima for Solar Cycles 12–23 (except the end of data for Solar Cycle 24). (NGDC, 2013).

Sunspot cycle number	Fractional year of minimum	Year and month of minimum	Cycle length [years]
18	1944.1	1944 February	10.2
19	1954.3	1954 April	10.5
20	1964.8	1964 October	11.7
21	1976.5	1976 June	10.2
22	1986.7	1986 September	10.1
23	1996.8	1996 October	12.2
24	2009.0	2008 December	10.9
25	2020	2019 December	

under 30 (Rybanský, 1975; Rybanský, Rušin, and Minarovjech, 2001; Rybanský et al., 2005; Minarovjech, Rušin, and Saniga, 2011a).

Recently, the coronal indices were corrected, mainly for the pre-1966 era. In this study we use the new, reconstructed coronal indices, which were downloaded from www.ngdc.noaa.gov/stp/solar/corona.html (Rybanský et al., 2005). The main period in this study is Solar Cycles 18–23, in order to have the same number of even and odd cycles. In some cases we also use data for Solar Cycle 24. These are downloaded from www.suh.sk/obs/vysl/MCI.htm (Lukáč and Rybanský, 2010).

2.2. Sunspot Groups

When plotting sunspot groups, we use the data set of sunspot groups, for Solar Cycles 18–24 from Leussu et al. (2017). This data set contains the latitude and time stamp of sunspot groups seen for the first time. This data set does not include the whole of Solar Cycle 24, but only to the end of 2016. The minima and length of the sunspot cycles used in this study for solar and also geomagnetic indices are listed in Table 1.

2.3. Two-Sample T-Test

The two-sample T-test for equal mean values is defined as follows. The null hypothesis assumes that the means of the populations are equal, i.e. $\mu_1 = \mu_2$. The alternative hypothesis is that $\mu_1 \neq \mu_2$. The test statistic is calculated as

$$T = \frac{\mu_1 - \mu_2}{\sqrt{s_1^2/N_1 + s_2^2/N_2}}, \tag{1}$$

where N_1 and N_2 are the sample sizes, μ_1 and μ_2 are the sample means, and s_1^2 and s_2^2 are the sample variances. If the variances of the populations are assumed equal, the formula reduces to

$$T = \frac{\mu_1 - \mu_2}{s_p\sqrt{1/N_1 + 1/N_2}}, \tag{2}$$

where

$$s_p^2 = \frac{(N_1 - 1)s_1^2 + (N_2 - 1)s_2^2}{N_1 + N_2 - 2}. \tag{3}$$

The rejection limit for the two-sided T-test is $|T| > t_{1-\alpha/2,\nu}$, where α denotes the significance level and ν the degrees of freedom. The values of $t_{1-\alpha/2,\nu}$ are published in T-distribution tables (Snedecor and Cochran, 1989; Krishnamoorthy, 2006; Derrick, Deirdre, and White, 2016). Now, if the value of $p < \alpha = 0.05$, the significance is at least 95%, and if $p < \alpha = 0.01$, the significance is at least 99%.

2.4. Principal Component Analysis Method

Principal component analysis is a useful tool in many fields of science including chemometrics (Bro and Smilde, 2014), data compression (Kumar, Rai, and Kumar, 2008), and information extraction (Hannachi, Jolliffe, and Stephenson, 2007). PCA finds combinations of variables that describe major trends in the data. PCA has earlier been applied, e.g., to studies of the geomagnetic field (Bhattacharyya and Okpala, 2015), geomagnetic activity (Holappa, Mursula, and Asikainen, 2014; Takalo, 2021b), the ionosphere (Lin, 2012), the solar background magnetic field (Zharkova et al., 2015), variability of the daily cosmic-ray count rates (Okpala and Okeke, 2014), and atmospheric correction to cosmic-ray detectors (Savić et al., 2019).

In this article we compare sunspot number (SSN) and solar 10.7 cm radio flux data (SRF) for Solar Cycles 19 – 24 to the same cycles of the coronal index of solar activity (CI). To this end, we estimate that the average length of the cycle is 130 months, and we use it as a representative solar cycle. We first resample the monthly data such that all cycles have the same length of 130 time steps (months), i.e. about the average length of the Solar Cycles 18 – 24 (Takalo and Mursula, 2018, 2020; Takalo, 2021b). This effectively elongates or shortens the cycles to the same length. Before applying the PCA method to the resampled cycles we standardize each individual cycle to have zero mean and unit standard deviation. This guarantees that all cycles will have the same weight in the study of their common shape. Then, after applying the PCA method to these resampled and standardized cycles, we revert the cycle lengths and amplitudes to their original values.

Standardized data are then collected into the columns of the matrix X, which can be decomposed as (Hannachi, Jolliffe, and Stephenson, 2007; Holappa et al., 2014; Takalo and Mursula, 2018)

$$X = U \, D \, V^T \,, \tag{4}$$

where U and V are orthogonal matrices, V^T is the transpose of matrix V, and D is a diagonal matrix $D = diag(\lambda_1, \lambda_2, \ldots, \lambda_n)$ with λ_i the ith singular value of matrix X. The principal components are obtained as the column vectors of

$$P = U D. \tag{5}$$

The column vectors of the matrix V are called empirical orthogonal functions (EOF), and they represent the weights of each principal component in the decomposition of the original normalized data of each cycle X_i, which can be approximated as

$$X_i = \sum_{j=1}^{N} P_{ij} \, V_{ij} \,, \tag{6}$$

where j denotes the jth principal component (PC). The explained variance of each PC is proportional to the square of the corresponding singular value λ_i. Hence, the ith PC explains

a percentage

$$\frac{\lambda_i^2}{\sum_{k=1}^n \lambda_k^2} \, 100\% \tag{7}$$

of the variance in the data.

3. Homogeneous Coronal Data Set

Figure 1 shows the sunspot groups and homogeneous coronal data set (HCDS) indices (Minarovjech, Rušin, and Saniga, 2011b) separately for the Solar Cycles 18 – 24. The intensity of these coronas are shown as a color bar on the right side of the Cycle 24 panel. It seems that the most intense corona is around the maximum for Cycles 19 and 22, but the most intense values are spread more widely for the other cycles. Note also that the largest sunspots are concentrated around the maximum for the Cycles 19 and 22, but they are more abundant in the descending phase for other cycles, especially so for the Cycle 21. The maxima of the cycles are depicted with a vertical white line. The database used contains an incomplete Cycle 24 and has groups only to the end of the year 2016 (Leussu et al., 2017).

Figures 2a and b show the lines of average HCDS indices of the east limbs of the Sun as a function of day of the average even cycle for the northern and southern hemisphere of the Sun, respectively. The lines with five-degree separation are arranged such that the lowest lines are at the Poles and the highest lines are near the Equator of the Sun. The red arrows show the drift of the latitudinal maximum towards the Poles. The maximum HCDS corona maximum appears first around 1000 days, i.e. about a quarter of the way through cycles near 40 – 50 degrees northern latitude and somewhat later in the southern hemisphere at corresponding latitudes. The maxima appear at the Pole around 1200 days and 1350 days after the start of the cycle for the northern and southern hemisphere, respectively (Minarovjech, Rušin, and Saniga, 2011a). A similar drift, but stronger, appears towards the Equator in both hemispheres. These reach their maxima at about 2000 days, i.e. at the halfway point of the cycle. Note, however, that there exists another, local maximum at about 1560 days after the start of the cycle, and there is a gap between these two maxima. We believe that this is related to the Gnevyshev gap. For odd cycles, the migration of the latitudinal maximum is similar, although somewhat more complex. This is probably due to the huge difference in the distribution of the HCDS corona for odd cycles. For example, Cycle 21 has two maxima at the North Pole, the first at 1350 days and another late in the descending phase at about 2500 days after the start of the cycle. Figure 3 confirms that Cycles 19 and 22 are quite symmetric around the maximum in the number of strong HCDS corona (>150) events. Note also that Cycle 24 has only 19 strong corona events, and all of those are before the maximum in April 2014.

Figure 4 shows the maximum (blue) and average (red) values of HCDS corona for Solar Cycles 18 – 23 in Cartesian (Figure 4a) and polar (Figure 4b) coordinates. The left and right sides of the figure (here and in the succeeding figures) show the values at the east and west limb of the Sun, respectively. It is evident that the absolute values of the maxima are all between 15 – 20 degrees of heliographic latitude. These latitudes are somewhat larger than the maxima of the sunspot distributions, which are between 14.9 and 15.5 for even and odd cycles, respectively (Takalo, 2020). The overall values of the corona are slightly stronger for the northern hemisphere than the southern hemisphere. The issue of northern/southern hemisphere asymmetry is, however, more complicated than this simple figure displays, (see,
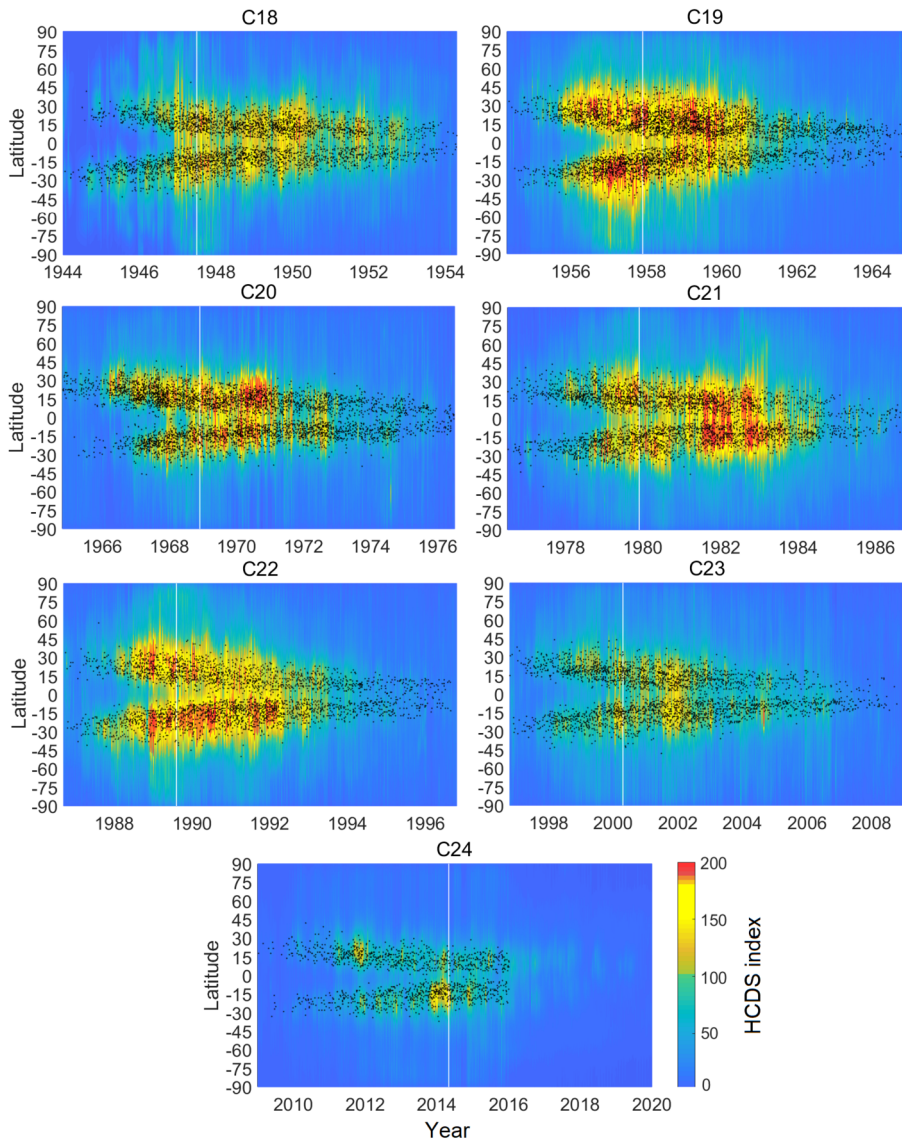
Figure 1 Homogeneous corona data set (*color bar*) and sunspot groups (*black dots*) separately for Solar Cycles 18 – 24. The *white vertical lines* show the maxima of the cycles. (Note that sunspots for 2017 – 2019 are missing from the database used.)

e.g., Dzifčáková and Rušin (1998) and Joshi et al. (2015)). Figure 5 shows the latitudinal distribution of the HCDS corona for even and odd cycles separately. It is notable that Cycles 19 and 22 are the most asymmetrical, such that the northern hemisphere is dominating for Cycle 19 and the southern hemisphere is dominating for Cycle 22. These are also the cycles that were mentioned earlier as the most symmetric around the maximum for strong corona events. The coronal values for Solar Cycles 23 and 24 are understandably far smaller than for the other cycles.
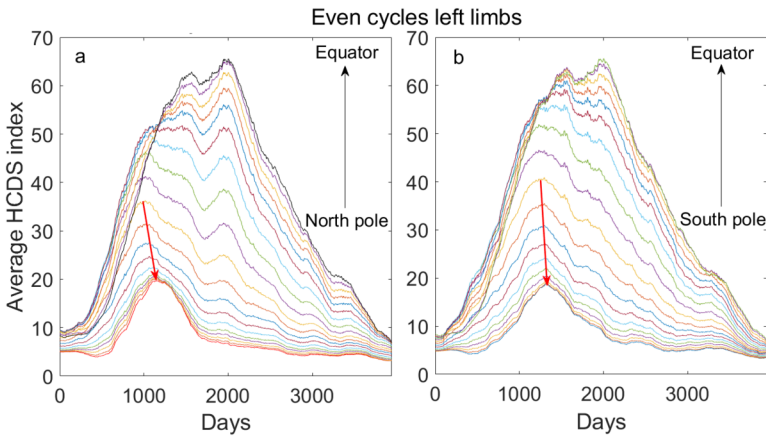
Figure 2 The lines (with five-degree resolution) of the average HCDS indices in the east limb of the Sun as a function of day for the average even cycle. The lines are arranged such that the lowest lines are at the Poles and the highest lines at the Equator. The *red arrows* show the temporal drift of the latitudinal maxima towards the Poles. Panels **a** and **b** are for the northern and southern hemisphere, respectively.

Figure 3 Number of HCDS indices greater than 150 for the Cycles 18 – 24. The *black vertical lines* show the maxima of the cycles.
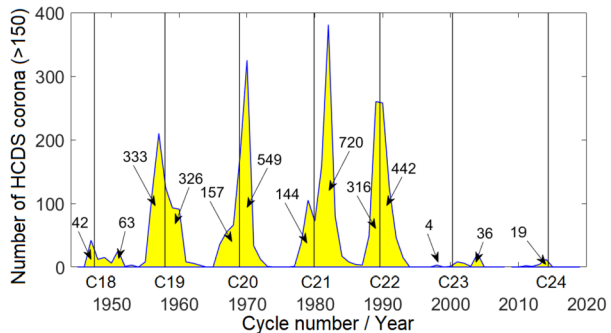
Figure 6 shows the maximum (yellow) and average (red) HCDS corona every second year for Solar Cycle 21. The starting and ending minima for this cycle were June 1976 and September 1986, and the maximum was December at the turn of the years 1979 – 80. The diagrams for 1976 and 1986 are calculated only for the partial years. As already seen from Figure 1, the coronal maximum is not in 1980, but 1982, i.e. in the descending phase of the cycle. Another interesting feature is in the year 1984 diagrams. There are only two maxima in the average corona and both in the southern hemisphere. The maximum corona, however, exhibits peaks for both hemispheres.

Figures 7a and 7b show the number of different sizes of HCDS corona and the total strength of these categories as a function of heliographic latitude on the east limb of the Sun for Cycles 18 – 23 (we do not show here the west limb because the distributions are understandably very similar). It is clear that the amount (Figure 7a) of the faintest corona (<15) is by far the largest, except at the zones between $15 – 20$ and -15 to -20 of heliographic latitude. Furthermore, the amount of weak corona increases towards the Poles in both hemispheres. The latitudinal corona values between $15 – 30$ are most abundant at 50 (-50) degrees of heliographic latitude and also have a local maximum at the solar Equator. The next category ($30 – 45$) is almost constant between latitudes -30 – 30 and decreases towards the Poles. The
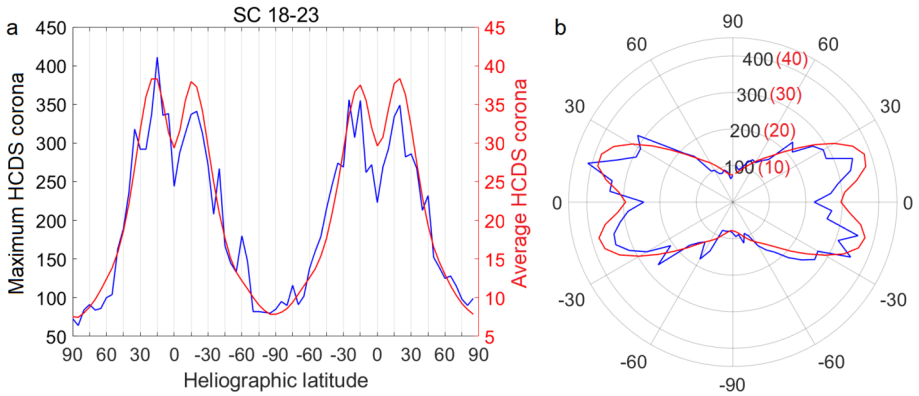
Figure 4 The maximum (*blue, left vertical axis*) and average values (*red, right vertical axis*) of HCDS for Solar Cycles 18 – 23 (**a**) in Cartesian coordinates, and (**b**) in polar coordinates. (Note that for polar coordinates the *maximum is the black value* and the *average is the red value*.)
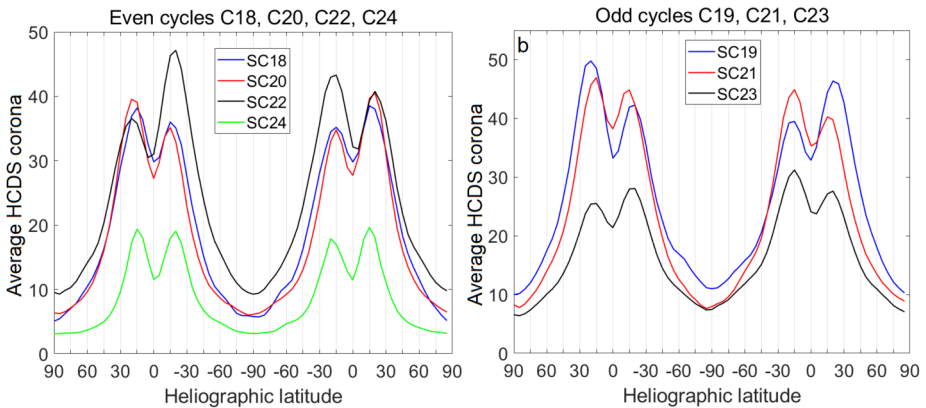

Figure 5 The average values of latitudinal (HCDS) corona for Solar Cycles 18 – 24 (**a**) for even cycles, and (**b**) for odd cycles.

strongest corona values (≥ 45) are located mostly on the sunspot regions having maxima at the latitudes $15 - 20$ and $-15 - -20$. Figure 7b shows that, when calculating the total intensity of the categories, the strongest corona is dominating at the sunspot zone, i.e. between $-45 - 45$ degrees of latitude.

Vernova, Tyasti, and Baranov (2016) have studied the photospheric magnetic-field distributions for Solar Cycles $21 - 23$ in different categories of the magnetic-field intensity (see also Rušin and Rybanský (2002)). Figure 8 shows the distribution of the flux of the strongest photospheric magnetic fields ($B > 50$ Gauss) as a green curve (the y-axis also as green on the right side, in Maxwells, which is used in the article of Vernova, Tyasti, and Baranov (2016)). This distribution is very similar to the distribution of the total strength of the strongest HCDS corona events (> 100, shown as red color) and the histogram of the number of sunspot groups as a function of heliographic latitude (y-axis left). It should, however, be noted that a field strength of $0 - 5$ Gauss occupied more than 60% of the solar surface in $1976 - 2003$, while strong fields ($B > 50$ Gauss) occupied 3.3% of the solar surface (see Vernova, Tyasti, and
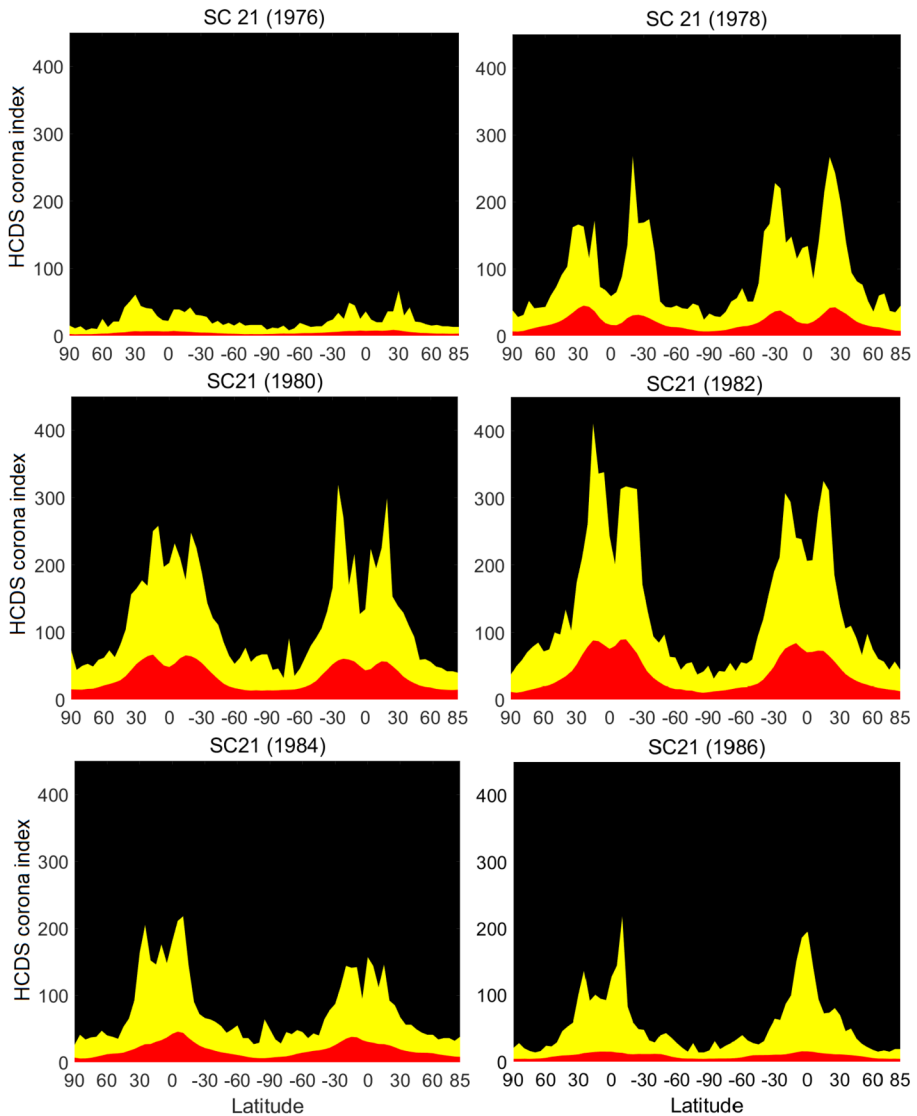
Figure 6 The maximum (*yellow*) and average (*red*) HCDS corona every second year for Solar Cycle 21.

Baranov (2016)). It is interesting that the distribution of the flux of the faintest, i.e. the most abundant (35–80% of the time) photospheric magnetic field ($B=0-5$ Gauss), has a similar shape to the distribution of amount of the latitudinal corona between $10-25$. Figure 9 shows the distribution of the amount of corona (blue) and photospheric magnetic flux (red) in Mx for these categories. Both of the curves have maxima at absolute values $50-55$ and a smaller maximum at the Equator of the Sun.
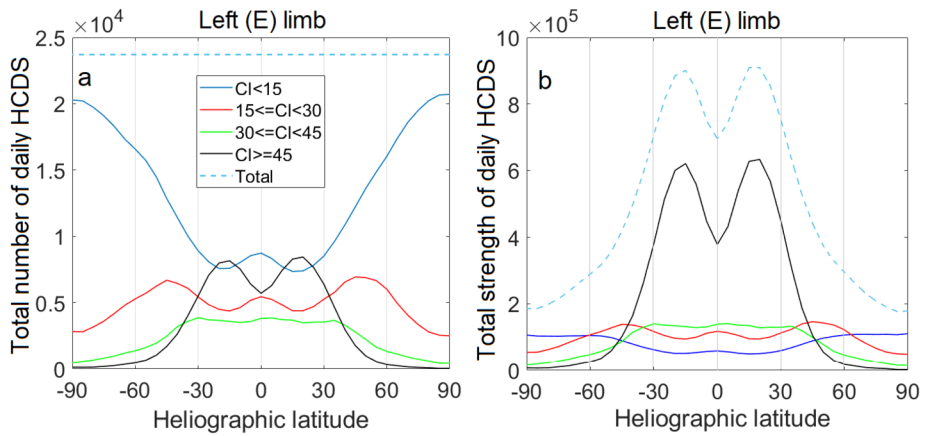
Figure 7 (**a**) The amount of different category HCDS coronas (marked in the legend as CI) and (**b**) the distributions of total strength of the categories as a function of heliographic latitude.

Figure 8 Number of HCDS corona events (>100, *red*) and photospheric magnetic flux (*green*) in Maxwells [Mx] for magnetic fields greater than 50 Gauss together with a histogram of sunspot groups.
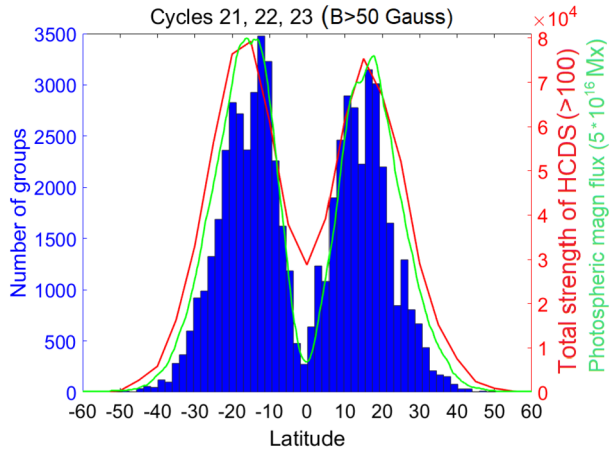
4. Coronal Index of Solar Activity (CI)

4.1. The Average-Shape CI Cycle

Figure 10 shows the monthly mean values of the coronal index of solar activity (CI) for even and odd cycles between SC18 – SC23, respectively. All of the cycles are here resampled to have the same length of 130 time steps (months), which is about the average length of Solar Cycles 18 – 24. The shape of the monthly CI is very similar to the sunspot cycle with an ascending phase of about three years, a quite flat top, and a five-and-a-half-year descending phase on the average. There is a good candidate for GG in the even cycles between 51 – 60 months, i.e. about 40% from the start of the cycle. We calculated that the two-sample T-test gives significance for the difference of the means in the interval 51 – 60 time steps compared to intervals 41 – 50 and 61 – 65 (note that the descending phase starts at about 65 time steps) with $p = 8.7 \times 10^{-5}$. This means that the significance is better than 99% for even cycles. The drop seen in odd cycles between 45 – 50, i.e. about 37% from the preceding minimum, is

Figure 9 Number of HCDS corona events between $10-25$ (*blue*) and photospheric magnetic flux (*red*) in Mx for magnetic fields between $0-5$ Gauss.
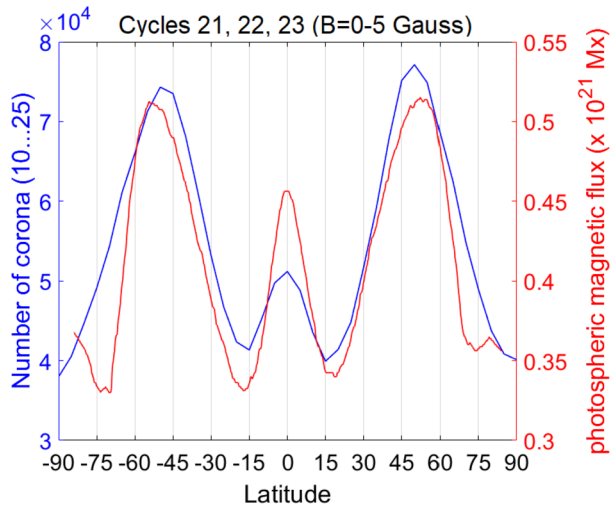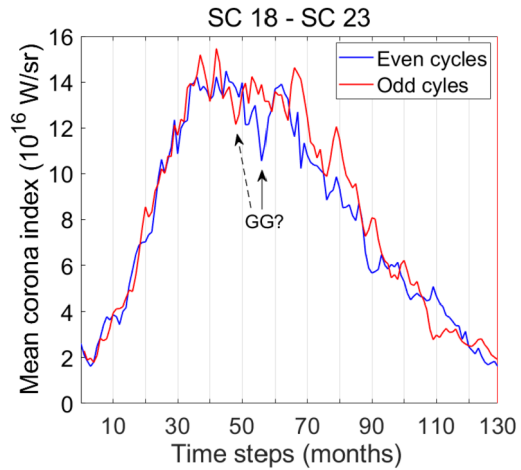

Figure 10 Average monthly CI for even and odd cycles for SC18 $-$ SC23.

less conspicuous (dashed arrow). However, the mean between $47-50$ months is significant at the 95% level with $p=0.025$ for four months compared to similar intervals before and after the gap.

In order to study the relevance of the supposed GG in more detail, we use daily values of CI and calculate how many daily values are greater/less than half of the largest corona value (24.06) during the period of Cycles $18-23$. Figures 11a and 11b show the histograms of daily CI values for even and odd cycles, respectively. We have resampled the daily values to 3950 days, which is about 130 months or 10.8 years, which is the average length of Solar Cycles $18-23$. In Figure 11a the CI values of even cycles less than or equal to 12 are shown as blue bars (*y*-axis as reversed on the left) and values over 12 as red bars (*y*-axis on the right). Each bar represents 50 days and because each day has one value the maximum is 50. In the middle of the maximum, i.e. with all values over 12, there is a deep gap with only a few large (>12) daily CI values (marked with white vertical lines in the figure). The deepest phase for this lasts over three months, but the decrease starts maybe another
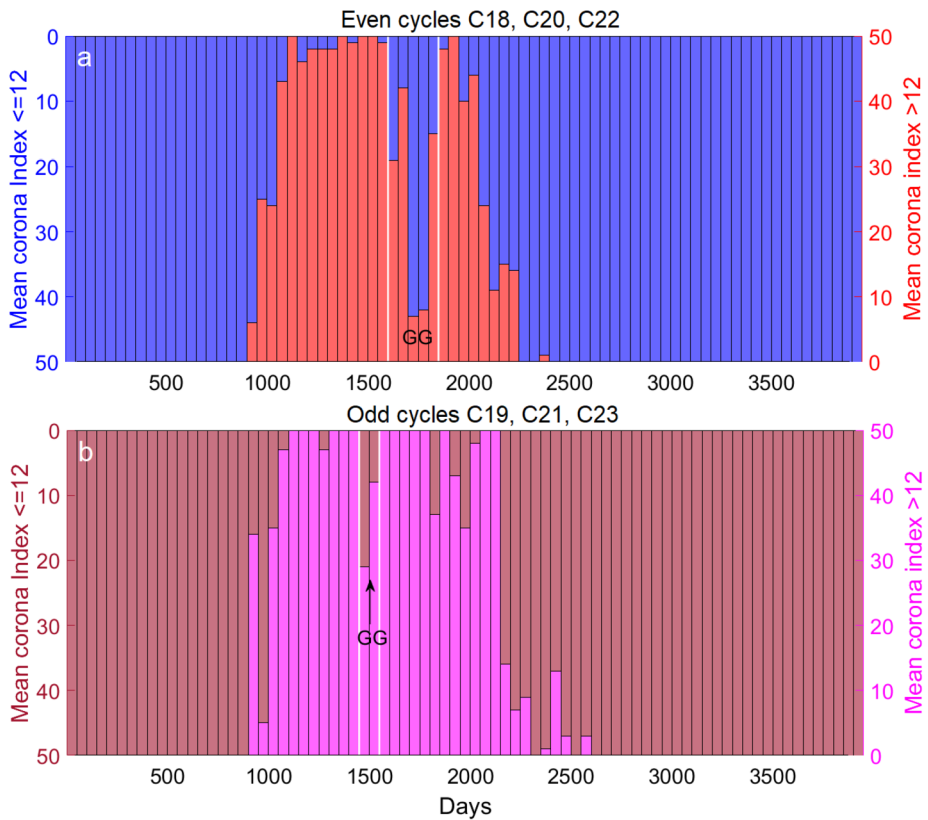
Figure 11 The number of CI values ≤ 12 or >12 as a histogram for (**a**) even and (**b**) odd cycles between SC18 – SC23. In Panel **a**, *blue* means CI ≤ 12 and *red* means CI > 12. In Panel **b**, *light-brown* means CI $\leq$ 12 and *magenta color* means CI > 12. Note that bars running from bottom to top with the same color mean that all 50 days of that bar are similar, i.e. all days ≤ 12 or all days > 12.

two months earlier. We have estimated using the two-sample T-test that the mean value of the gap between the white lines ($\approx$ eight months) has a significantly different mean value (at the 99% level) with $p = 0.0011$ compared to an equal period before or after the gap. We suppose that the period between the white lines is related to the Gnevyshev gap (GG, marked in the Figure 11a). The gap is about 40% from the preceding minimum of the average solar cycle. Note also the similarity of the average even cycle in Figure 10 and the histogram of Figure 11a for even cycles. There exists first a smaller drop and then a deeper gap in both diagrams.

In Figure 11b for odd cycles, the values under 12 are shown as light-brown bars and values over 12 with magenta bars. Now, the gap is somewhat earlier (37% from the preceding minimum) and shorter ($\approx$ 3 months). Although the T-test gives again 95% significance for the different mean, the result is somewhat suspicious, because there are only two values in the gap. Both of these results are, however, very well in line with the earlier results for the GG (Takalo and Mursula, 2020; Takalo, 2021c,a).

4.2. PCA of CI for Cycles 19 – 24

We have carried out the principal component analysis by equalizing the CI Cycles to 130 time steps (months) to obtain the two main principal components (PC) shown in Figure 12a. The first and second PC explain 87.8% and 7.3% of the total variation of the CI period C19 – C24, i.e. together 95.1% of the variation. The remaining four PCs account only for 4.9% of the variation and are usually just explaining some special feature of an individual cycle. The corresponding EOFs are shown in Figure 12b. According to the theory of PCA, PC1 should show the average shape of the cycles for the studied interval. The PC2 acts to correct the shape of the cycle when the corresponding cycle differs from the average cycle shape. The main effect of the PC2 is to reduce (positive scaling for PC2) or enhance (negative scaling for PC2) the activity level of the declining phase with respect to the ascending phase of the cycle (Takalo and Mursula, 2018). Positive (negative) scaling of PC2 means that it has positive (negative) phase in the first half of the cycle and negative (positive) phase in the second half of the cycle. Now, looking at the EOFs of Figure 12b it shows that the CI Cycle 21 differs from all the other cycles such that it has least weight to the PC1 (its EOF1 is smallest), but by far the highest (but negative) weight in its EOF2. We then returned each cycle to its original length, and back to its original amplitude, by multiplying both PCs with the standard deviation of the original cycle and adding the mean value of the original cycle to PC1. Then, we concatenated the cycles to their original order and obtained the full PC1 and PC2 series of Cycles 19 – 24. These two time series are shown in Figure 13a. Note that indeed the CI Cycle 21 has the highest amplitude in PC2 time series with negative phase in the first half and positive phase in the latter half of the cycle. The peak-to-peak variation of PC2 for the Cycle 21 is more than half of the height of the PC1 for that cycle. This confirms the characteristic of the CI Cycle 21 of Figures 1 and 2. The corona (both HCDS and CI) is strongly enhanced in the descending phase of Cycle 21. Cycles 20 and 24 have only slightly negative scaling. The other cycles, i.e. C19, C22, and C23, have positive scaling, meaning that the first half, i.e. the ascending phase of these cycles has a stronger corona than the average cycle. Figures 13b and 13c show similar PC analyses for sunspot number (SSN) and solar 10.7 cm radio flux (SRF) data for Cycles 19 – 24, respectively. (The reason why we study only Cycles 19 – 24 is that SRF data do not exist for the whole of Cycle 18.) It is evident that these data have quite similar PC2 time series with the same phases as the CI index, although the strength of the peak-to-peak variation changes somewhat. Note that the PC2 of Cycle 20 for all three data sets is almost a zero line, meaning that the PC1 is a kind of "model" cycle of these data for the interval C19 – C24. The variation PC2 for CI Cycle 24 is also quite minimal, although it fluctuates quite a lot with negative scaling for SSN and SRF. Note also that the variation of the PC2 of Cycle 21 is much weaker for SSN and SRF than for CI. There is a kind of 22-year (Hale cycle) anticorrelation, such that PC2 of CI has positive scaling for Cycle 19 (more weight on the first half of the cycle), negative scaling for Cycle 21 (more weight on the latter half), and again positive scaling for Cycle 23 (more weight on the first half). Similarly, C20, C22, and C24 have negative, positive, and negative scaling, respectively. Figure 14 shows the autocorrelation functions (ACFs) of PC1 and PC2 of CI for Cycles 19 – 24. The ACF of PC1 shows, as expected, the maxima at the solar-cycle variation in CI. The PC2 is more complicated and shows maxima near 1.5 and 2.5 solar cycle periods. Interestingly, there is a deep minimum in ACF of PC2 at the Hale-cycle period (262 months or 21.8 years). This confirms the aforementioned anticorrelation with the Hale cycle in the CI.

Figure 12 (**a**) The PC1 and PC2 for coronal index of solar activity (CI). (**b**) The corresponding EOF1 and EOF2 for CI.
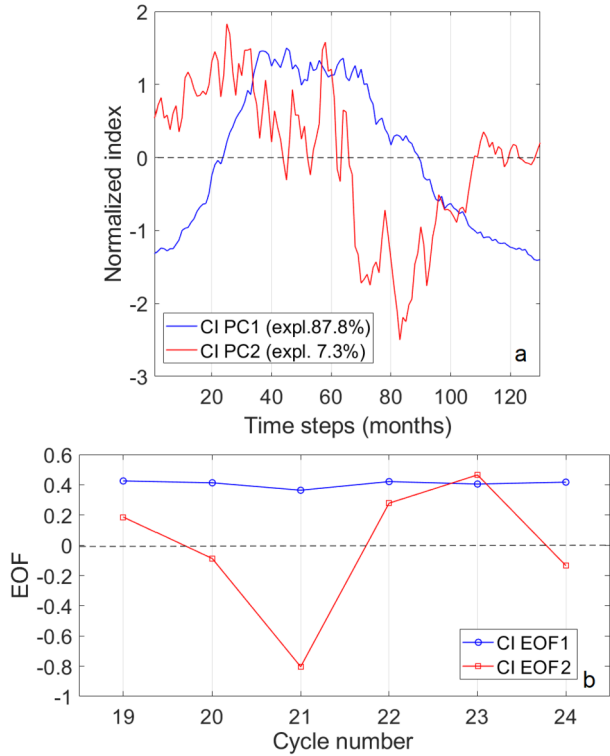
5. Conclusions

We found that the overall values of the homogeneous corona data set (HCDS) corona events are slightly stronger for the northern hemisphere than the southern hemisphere during Solar Cycles 18 – 23. It is noticeable that the Cycles 19 and 22 are most asymmetrical such that the northern hemisphere is dominating for Cycle 19 and the southern hemisphere is dominating for Cycle 22. These are, however, also the cycles that are the most symmetric around the cycle maximum for strong HCDS corona events. The coronal values for Solar Cycles 23 and 24 are understandably far smaller than for the other cycles.

The maximum HCDS corona maximum appears first around 1000 days, i.e. about a quarter after the start of the cycles near 40 – 50 degrees northern latitude and somewhat later in the southern hemisphere at corresponding latitudes. These maxima migrate towards the Poles such that they appear at the Pole around 1200 days and 1350 days after the start of the cycle for the northern and southern hemisphere, respectively. The equatorward drifts reach the low latitudes at about half of the cycle, and the maximum is clearly double peaked for the average even cycle.

The amount of weak HCDS corona increases towards the Poles in both hemispheres. The corona values between 15 – 30 are most abundant at 50 (-50) degrees of heliographic latitude and also have a local maximum at the solar equator. The next category (30 – 45) is almost constant between latitudes -30 – 30 and decreases towards the Poles. The strong HCDS corona (≥45) are located mostly on the sunspot regions having maxima at the absolute value of latitudes 15 – 20 in both hemispheres. When calculating the total intensity

Figure 13 (**a**) The PC1 and PC2 time series of CI for Cycles 19 – 24, (**b**) The PC1 and PC2 time series of SSN for Cycles 19 – 24. (**c**) The PC1 and PC2 time series of solar 10.7 cm radio flux for Cycles 19 – 24.
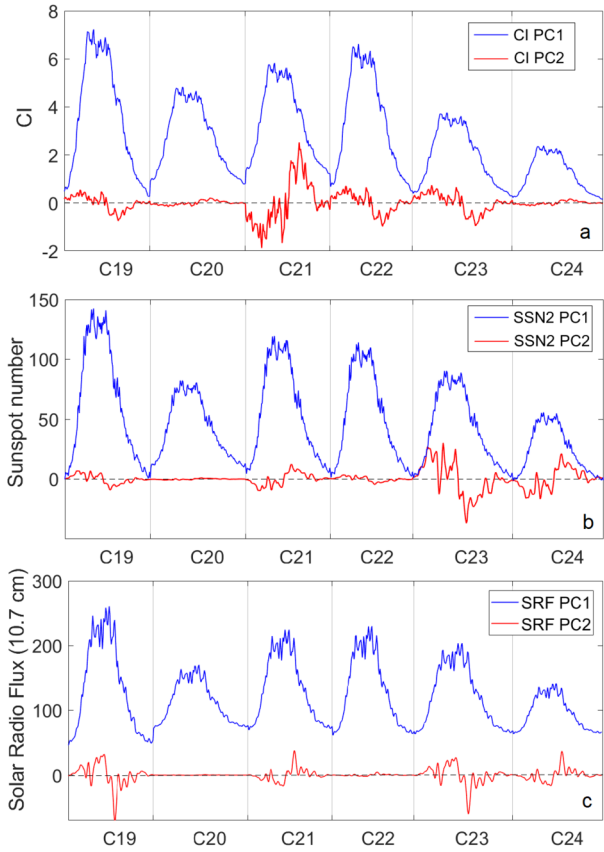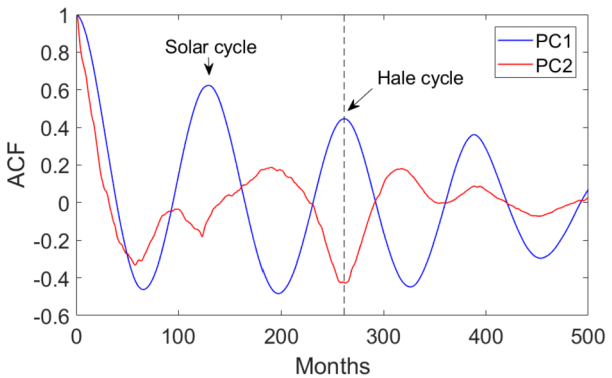
Figure 14 The autocorrelation functions of PC1 and PC2 time series of CI for Cycles 19 – 24. Note a deep minimum in the ACF of PC2 at the Hale-cycle period.

of the categories, the strong corona events are dominating at the sunspot zone, i.e. between -45 – 45 degrees of latitude.

The distribution of the flux of the strongest photospheric magnetic fields ($B > 50$ Gauss) is very similar to the distribution of the total strength of the strongest corona events (HCDS > 100) and the histogram of the number of sunspot groups. It should, however, be noted that the strongest magnetic field is very rare in the photosphere.

We found the Gnevyshev gap in the coronal index of solar activity (CI) for the even cycles between $51 - 60$ months, i.e. about 40% from the start of the cycle. We calculated using the two-sample T-test at least 99% significance for the difference of the means in the interval $51 - 60$ time steps compared to intervals $41 - 50$ and $61 - 65$ with $p = 8.7 \times 10^{-5}$. We confirmed the existence of GG also for daily CI data.

For the odd cycles the GG exists a little earlier and is shorter than for the even cycles. Although the significance of the gap is at the 95% level for the odd cycles, its existence is not as significant for the odd cycles as for the even cycles.

We have carried out a principal component analysis (PCA) of the CI for Cycles $19 - 24$. The principal components PC1 and PC2 account for 87.7% and 7.3% of the total variation of the data. The PCA confirms that Cycle 21 is most different from other cycles in that its PC2 has a strong negative scaling, i.e. negative phase in the first half and positive phase in the latter half of the cycle. We compared the PC1 and PC2 of the CI to the PC1 and PC2 of sunspot numbers and solar 10.7 cm radio-flux data. We found that their PC2 resembles that of the PC2 for CI such that PC2 of CI and SSN2 are in phase for all cycles, and PC2 of CI and SRF are in phase, except for Cycles 20 and 22, whose PC2 is almost zero for SRF. Differ from the zero line.

Declarations

References

Ahluwalia, H.S., Kamide, Y.: 2004, Gnevyshev gap, Forbush decreases, ICMEs and solar wind electric field: relationships. *Adv. Space Res.* **35**, 2119. DOI.

Bazilevskaya, G.A., Makhmutov, V.S., Sladkova, A.I.: 2006, Gnevyshev gap effects in solar energetic particle activity. *Adv. Space Res.* **38**, 484. DOI.

Bhattacharyya, A., Okpala, K.C.: 2015, Principal components of quiet time temporal variability of equatorial and low-latitude geomagnetic fields. *J. Geophys. Res.* **120**, 8799. DOI.

Bro, R., Smilde, A.K.: 2014, Principal component analysis. *Anal. Methods* **6**, 2812.

Derrick, B., Deirdre, T., White, P.: 2016, Why Welch's test is Type I error robust. *Quant. Methods Psychol.* **12**, 30. DOI.

Du, Z.L.: 2015, Bimodal structure of the Solar Cycle. *Astrophys. J.* **804**, 15. DOI. ADS.

Dzifčáková, E., Rušin, V.: 1998, The North-South asymmetry in the Green Corona. *Stud. Geophys. Geod.* **42**, 101. DOI.

Feminella, F., Storini, M.: 1997, Large-scale dynamical phenomena during solar activity cycles. *Astron. Astrophys.* **322**, 311. ADS.

Gnevyshev, M.N.: 1967, On the 11-years cycle of solar activity. *Solar Phys.* **1**, 107. DOI. ADS.

Gnevyshev, M.N.: 1977, Essential features of the 11-year solar cycle. *Solar Phys.* **51**, 175. DOI. ADS.

Hannachi, A., Jolliffe, I.T., Stephenson, D.B.: 2007, Empirical orthogonal functions and related techniques in atmospheric science: a review. *Internat. J. Clim.* **27**, 1119. DOI.

Holappa, L., Mursula, K., Asikainen, T.: 2014, A new method to estimate annual solar wind parameters and contributions of different solar wind structures to geomagnetic activity. *J. Geophys. Res.* **119**, 9407. DOI. ADS.

Holappa, L., Mursula, K., Asikainen, T., Richardson, I.G.: 2014, Annual fractions of high-speed streams from principal component analysis of local geomagnetic activity. *J. Geophys. Res.* **119**, 4544. DOI. ADS.

Joshi, B., Bhattacharyya, R., Pandey, K.K., Kushwaha, U., Moon, Y.-J.: 2015, Evolutionary aspects and north-south asymmetry of soft X-ray flare index during solar cycles 21, 22, and 23. *Astron. Astrophys.* **582**, A4. DOI.

Kane, R.P.: 2008, Gnevyshev peaks and gaps for coronal mass ejections of different widths originating in different solar position angles. *Solar Phys.* **249**, 369. DOI.

Kane, R.P.: 2015, Solar cycle variation of coronal green line index. *Indian J. Radio Space Phys.* **44**, 122.

Krishnamoorthy, K.: 2006, *Handbook of Statistical Distributions with Applications* **128**, Chapman & Hall, London. ISBN 1-58488-635-8.

Kumar, D., Rai, C.S., Kumar, S.: 2008, Principal component analysis for data compression and face recognition. *INFOCOMP J. Comput. Sci.* **7**, 48.

Leussu, R., Usoskin, I.G., Senthamizh Pavai, V., Diercke, A., Arlt, R., Mursula, K.: 2017, VizieR Online Data Catalog: Butterfly diagram wings (Leussu+. *VizieR Online Data Catalog* 359. 2017.

Lin, J.-W.: 2012, Ionospheric total electron content seismo-perturbation after Japan's March 11, 2011, M=9.0 Tohoku earthquake under a geomagnetic storm; a nonlinear principal component analysis. *Astrophys. Space Sci.* **341**, 251. DOI.

Lukáč, B., Rybanský, M.: 2010, Modified coronal index of the solar activity. *Solar Phys.* **263**, 43. DOI. ADS.

Minarovjech, M., Rušin, V., Saniga, M.: 2011a, Synoptic charts of solar magnetic fields. *Contrib. Astron. Obs. Skaln. Pleso* **41**, 106. ADS.

Minarovjech, M., Rušin, V., Saniga, M.: 2011b, The green corona database and the coronal index of solar activity. *Contrib. Astron. Obs. Skaln. Pleso* **41**, 137. ADS.

NGDC: 2013, *Solar-indices*. National Geophysical Data Center (NGDC), Boulder, Colorado, USA. (https://www.ngdc.noaa.gov/stp/space-weather/solar-data/solar-indices/sunspot-numbers/cycle-data/table_cycle-dates_maximum-minimum.txt) from the National Geophysical Data

Norton, A.A., Gallagher, J.C.: 2010, Solar-cycle characteristics examined in separate hemispheres: phase, Gnevyshev Gap, and length of minimum. *Solar Phys.* **261**, 193. DOI. ADS.

Okpala, K., Okeke, F.: 2014, Variability of the Daily Cosmic Ray Count rates in the Northern Hemisphere. Willis, P. (ed.): In: 40th COSPAR Sci. Ass. **40**, D1.3

Rušin, V., Rybanský, M.: 2002, The Green Corona and magnetic fields. *Solar Phys.* **207**, 47. DOI. ADS.

Rybanský, M.: 1975, Coronal index of solar activity. I - Line 5303 A, year 1971. II - Line 5303 A, years 1972 and 1973. *Bull. Astron. Inst. Czech.* **26**, 367. 1973.

Rybanský, M., Rušin, V., Minarovjech, M.: 2001, Coronal index of solar activity - Solar-terrestrial research. *Space Sci. Rev.* **95**, 227. ADS.

Rybanský, M., Rušin, V., Minarovjech, M., Klocok, L., Cliver, E.W.: 2005, Reexamination of the coronal index of solar activity. *J. Geophys. Res., Space Phys.* **110**, A08106. DOI. ADS.

Savić, M., Dragić, A., Maletić, D., Veselinović, N., Banjanac, R., Joković, D., Udovičić, V.: 2019, A novel method for atmospheric correction of cosmic-ray data based on principal component analysis. *Astropart. Phys.* **109**, 1.

Snedecor, G.W., Cochran, W.G.: 1989, *Statistical Methods* **64**, 8th edn. Iowa State University Press, Ames. ISBN 978-0-8138-1561-9/89

Takalo, J.: 2020, Comparison of latitude distribution and evolution of even and odd sunspot cycles. *Solar Phys.* **295**, 49. DOI.

Takalo, J.: 2021a, Comparison of geomagnetic indices during even and odd solar cycles SC17-SC24: signatures of Gnevyshev gap in geomagnetic activity. *Solar Phys.* **296**, 19. DOI.

Takalo, J.: 2021b, Separating the aa-index into solar and hale cycle related components using principal component analysis. *Solar Phys.* **296**, 80. DOI.

Takalo, J.: 2021c, Temporal distribution of solar cycle 24 sunspot groups: comparison to cycles 12-23. *Ann. Geophys.* **64**, 1. DOI.

Takalo, J., Mursula, K.: 2018, Principal component analysis of sunspot cycle shape. *Astron. Astrophys.* **620**, A100. DOI.

Takalo, J., Mursula, K.: 2020, Comparison of the shape and temporal evolution of even and odd solar cycles. *Astron. Astrophys.* **636**, A11. DOI.

Vernova, E.S., Tyasti, M.I., Baranov, D.G.: 2016, Latitudinal distribution of photospheric magnetic fields of different magnitudes. *Solar Phys.* **291**, 741. DOI.

Waldmeier, M.: 1957, *Die Sonnenkorona, Struktur und Variationen der Monochromatischen Korona*, Birkhäuser, Basel.

Zharkova, V.V., Shepherd, S.J., Popova, E., Zharkov, S.I.: 2015, Heartbeat of the sun from principal component analysis and prediction of solar activity on a millenium timescale. *Nature Sci. Rep.* **5**, 15689. DOI. ADS.